

Effect of thermal ageing on creep and oxidation behaviour of Type 316H stainless steel

B. Chen, J. N. Hu, P. E. J. Flewitt, A. C. F. Cocks, R. A. Ainsworth, D. J. Smith, D. W. Dean & F. Scenini

To cite this article: B. Chen, J. N. Hu, P. E. J. Flewitt, A. C. F. Cocks, R. A. Ainsworth, D. J. Smith, D. W. Dean & F. Scenini (2015) Effect of thermal ageing on creep and oxidation behaviour of Type 316H stainless steel, Materials at High Temperatures, 32:6, 592-606, DOI: [10.1179/1878641315Y.0000000005](https://doi.org/10.1179/1878641315Y.0000000005)

To link to this article: <https://doi.org/10.1179/1878641315Y.0000000005>



Published online: 21 Apr 2015.



Submit your article to this journal [↗](#)



Article views: 767



View related articles [↗](#)



View Crossmark data [↗](#)



Citing articles: 4 View citing articles [↗](#)

Effect of thermal ageing on creep and oxidation behaviour of Type 316H stainless steel

B. Chen^{*1}, J. N. Hu², P. E. J. Flewitt³, A. C. F. Cocks², R. A. Ainsworth⁴,
D. J. Smith⁵, D. W. Dean⁶ and F. Scenini¹

The UK has unique experience in operating high temperature civil nuclear power systems, known as advanced gas cooled reactors (AGRs). One of the primary challenges for extending the lifetime of the AGR power stations is to understand the interaction that occurs between the AGR CO₂ environment and creep-fatigue cracking behaviour. This is one of the life limiting degradation mechanisms for steel components within the reactor pressure vessel. This paper addresses the effect of thermal aging on material internal state that controls both the creep deformation and oxidation behaviour of Type 316H stainless steels when they are exposed at a simulated AGR environment. Experimental results from creep tests are discussed with respect to a multi-scale self-consistent model, while experimental results from oxidation tests are considered with respect to the application of measured short term data to predict the long term oxidation behaviour. Finally, the interaction between oxidation and creep and its impact on high temperature structural integrity of AGR nuclear systems are discussed.

Keywords: Creep, Oxidation, Neutron diffraction, Crystal plasticity, Austenitic stainless steel, Gas cooled reactor

Introduction

There are 14 advanced gas cooled reactors (AGRs) at seven sites across the UK. They were constructed in the period from the late 1960s to the late 1980s. Some of the AGRs have operated for over 35 years, which is in excess of their original design lives of 25 or 30 years. One of the major challenges in extending the lives of elevated temperature plant components is to understand the changes in the microstructure of the structural materials arising from thermal aging over such extended periods of operation (up to ~40 years). These changes are further influenced by the stresses, environment and neutron irradiation. It is necessary for nuclear plant operators to understand these changes to ensure that throughout the service life the plant continues to fulfil the design intent.^{1,2}

Type 316H austenitic stainless steel, as one of the structural materials used in AGR boiler superheaters, has been exposed at temperatures ranging from 470 to 530°C in an AGR (predominantly carbon dioxide) environment. Progressive changes in the underlying microstructure of the material are observed over the high temperature service life. For example,

metallurgically the amount and type of second-phase precipitation lead to changes in the composition of the austenite matrix.³ In addition, internal misfit strains/stresses between grains can be created as a consequence of elastic-plastic anisotropy, as revealed by many *in situ* neutron diffraction studies.⁴⁻⁶ The coolant gas used in the AGR pressure circuit is predominantly carbon dioxide (CO₂), which also contains proportions of carbon monoxide (CO), hydrogen (H₂), methane (CH₄) and water vapour (H₂O).⁷ Therefore, it is important to understand the interaction that occurs between the AGR CO₂ environment and creep-fatigue cracking behaviour, which is one of the life limiting degradation mechanisms for steel components within the reactor pressure vessel.⁸ Recent findings⁸ suggest a synergistic relationship, which is not entirely understood; thus this could lead to undermining the current high temperature structural integrity assessment procedures.⁹ If we consider these complex microstructural changes as an overall manifestation of internal state, then the external state includes temperature, pressure and chemistry of the coolant gas.

In general, the changes in material internal state over the service life of a component can have a detrimental impact on several mechanical and physical parameters including both creep¹⁰ and oxidation properties.¹¹ For instance, it has been demonstrated by Chen *et al.*¹² that the rate of stress relaxation driven by creep deformation is dependent on the concentration of the solute elements in the matrix of Type 316H stainless steel. It has been also demonstrated that solution annealed (SA) specimens have a higher resistance to creep deformation than thermally aged specimens. This is for Type 316H stainless steel uniaxial creep specimens tested at 550°C and

¹School of Materials, The University of Manchester, Manchester M13 9PL, UK

²Department of Engineering Science, University of Oxford OX1 3PJ, UK

³H. H. Wills Physics Laboratory, University of Bristol, Tyndall Avenue, Bristol BS8 1TL, UK

⁴School of Mechanical, Aerospace & Civil Engineering, The University of Manchester, Manchester M13 9PL, UK

⁵Department of Mechanical Engineering, University of Bristol, Bristol BS8 1TR, UK

⁶EDF Energy Nuclear Generation Ltd., GL4 3RS, Gloucester, UK

*Corresponding author, email bo.chen-2@manchester.ac.uk

250 MPa.⁵ Another example relates to how thermal aging modifies oxidation behaviour in a wet CO₂ environment at 400°C for both SA and thermally aged Type 304 stainless steels.¹¹ In this case, the measured oxidation rate of the thermally aged Type 304 stainless steel was four times that of the SA material. This difference has been attributed to the presence of second-phase precipitates at grain boundaries in the thermally aged Type 304 stainless steel.¹¹

Confidence in high temperature structural integrity assessment methods, such as the UK's R5 procedures, is obtained by using conservative material property data over the required service life.⁹ Thus, it is essential to be able to either monitor or model the microstructural changes that occur over the service life. Moreover it is important to develop experimental techniques that can be used to quantify the changes in material internal state so that they can be incorporated into the R5 procedures. Because experimental data are often obtained from accelerated laboratory tests, limitations are encountered for predicting the material behaviour beyond the duration of test data. Thus a mechanistic-based model is preferred for extrapolation rather than a phenomenologically based one. In this paper, results from recent studies obtained by Bristol, Manchester and Oxford universities are presented. These have been carried out in support of lifetime extension of the UK's AGR reactors. The focus of this paper is to understand the effects of thermal aging on both creep and oxidation properties of a Type 316H austenitic stainless steel and to consider the implications of their interactions on structural integrity assessment.

Material

Material for creep tests

Thermally aged (ex-service) Type 316H austenitic stainless steel was provided by EDF Energy Generation Ltd. This had been removed from an ex-service (EX) AGR superheater header (about 65 mm wall thickness). H1 is the abbreviation for this header material. The chemical composition of this header material is given in Table 1. This material had been in service for 65,015 h at temperatures between 490 and 530°C. This was followed by further thermal aging at 550°C for 22,100 h in a laboratory furnace. Thus the microstructural condition is named as EX plus laboratory thermally aged material (EXLA). A solution heat treatment at 1090°C for 2.5 h followed by water quenching was given to this header material to produce a SA microstructural condition. This heat treatment should not change the chemical composition of the material. Grain sizes for both EXLA and SA microstructural conditions were found to be 87 ± 9 and 85 ± 10 μm (mean linear intercept), respectively.⁵ Creep deformation studies, described in 'Creep'

section, were carried out on H1 header material with both the EXLA and SA microstructural conditions.

Material for oxidation tests

A Type 316H stainless steel that had been subjected to plant service for 98,704 h at temperatures between 490 and 530°C was provided by EDF Energy Generation Ltd. This had been removed from an EX AGR superheater header (about 65 mm wall thickness). H2 is the abbreviation for this header material. The chemical composition is given in Table 1. The grain size of this material was measured to be 76 ± 11 μm (mean linear intercept). This EX material, representative of the thermally aged microstructural condition, was used to evaluate the oxidation behaviour. In addition, a SA Type 316H stainless steel tube (about 4 mm wall thickness) was provided by EDF Energy Generation Ltd. T is the abbreviation for this tube material. The chemical composition is given in Table 1. A solution heat treatment was undertaken at 1100°C for 3 min followed by water cooling to ambient temperature. The grain size of this material was measured to be 34 ± 4 μm (mean linear intercept), and it was used to evaluate the oxidation behaviour for SA microstructural condition (Table 1). Oxidation behaviour studies will be described in 'Oxidation' section.

Experimental

Microstructural characterisation

Several transmission electron microscopy (TEM) slices between 600 and 700 μm thick were cut from the bulk Type 316H stainless steels in the EX and SA microstructural conditions (Table 1). Specimens were mechanically ground to 100 μm thick by using both 400-grit and 800-grit SiC abrasive papers. Several 3 mm TEM discs were cutoff from each slice, followed by a further mechanical grinding using 1200-grit SiC abrasive papers. These 3 mm TEM discs were twin-jet electropolished using a solution with 80% perchloric acid and 20% methanol by using Struers' TenuPol-5 instrument. A Philips CM20 TEM, operating at 200 kV with a LaB6 filament, was used to observe the microstructure difference between EX and SA Type 316H stainless steels with a primary focus on the presence of second-phase precipitates and dislocation density and arrangement. A single tilt specimen holder was fitted with this TEM instrument. These TEM discs were then examined using FEI Quanta 650 field emission gun scanning electron microscopy (FEG-SEM). In this case, the thicker areas (away from the electron transparent areas) of the electropolished 3 mm TEM discs were examined by using FEG-SEM to evaluate the general microstructures for both the EX and SA Type 316H stainless steels.

Table 1 Chemical compositions of Type 316H austenitic stainless steels

Material ID	Microstructural condition	Type of test	Chemical composition/wt-%								
			C	Si	Mn	P	S	Cr	Mo	Ni	Fe
H1	EXLA and SA	Creep	0.06	0.40	1.98	0.021	0.014	17.2	2.20	11.83	Bal.
H2	EX	Oxidation	0.05	0.49	1.56	0.021	0.009	16.9	2.26	11.40	Bal.
T	SA	Oxidation	0.05	0.53	1.56	0.029	0.005	16.9	2.04	11.25	Bal.

H1: header material 1 for creep study; H2: header material 2 for oxidation study; T: tube material for oxidation study; EXLA: ex-service plus laboratory thermally aged; EX: ex-service; SA: solution annealed.

Creep

Uniaxial round bar specimens with a 28.25 mm gauge length and a 5.6 mm diameter were used for the creep tests. The creep strain of each specimen was measured by using two linear variable differential transducers. Both the EXLA and SA Type 316H stainless steel specimens (Table 1) were crept at 550°C with a range of applied tensile stresses from 250 to 320 MPa. The steady state true creep rate was determined when the secondary creep condition was achieved by each specimen. This provided a measure of creep stress exponent for these two microstructural conditions. In addition, several replicate test specimens for both the EXLA and SA conditions were crept at 550°C and under a stress of 250 MPa. These were deformed to different creep states, specimens 4–12, 14–16 and 18 in Table 2, then cooled from 550°C to room temperature, and finally unloaded. The creep states included (i) loading to an engineering stress of 250 MPa; (ii) loading and creep for 180 h in the primary creep regime; (iii) loading and creep for 1000 h to reach the secondary creep regime.

Room temperature *ex situ* neutron diffraction

High temperature pre-strained specimens (numbered 4–12 and 14–16 in Table 2) and non-prestrained reference specimens (numbered 1–3 and 13 in Table 2) were then measured by using the neutron diffraction instruments at both ENGIN-X, UK, and POLDI, Switzerland. Details of these two neutron diffraction instruments and the set-up of specimens have been described elsewhere.^{5,13,14} The neutron diffraction measurements were carried out along the axial direction of the specimens to quantify the axial internal misfit strains created by the pre-strain at 550°C. The internal misfit strains between grains in the pre-strained specimens were evaluated from the relative change of their lattice spacings

$$\varepsilon_{hkl} = \frac{d_{hkl} - d_{hkl}^0}{d_{hkl}^0} \quad (1)$$

where d_{hkl} is the lattice spacing measured on the pre-strained specimen, and d_{hkl}^0 is the stress-free lattice spacing measured on the reference specimen. For the EXLA

condition, specimens 1 and 2 were used for the stress-free reference of the ENGIN-X measurements, and specimen 3 was used as the stress-free reference for the POLDI measurements (Table 2). For the SA condition, specimen 13 was used for the stress-free reference of ENGIN-X measurements (Table 2). Four grain families were measured: {111}, {200}, {220} and {311}.

A gauge volume of $3 \times 3 \times 4$ mm was used to measure the lattice spacings throughout the ENGIN-X measurements. A typical measurement time of 540 s was selected to ensure good counting statistics for the diffraction peaks. A single peak fitting routine available at ENGIN-X was used to determine the specific lattice spacing.¹⁵ For the POLDI measurements, a larger gauge volume of $4 \times 4 \times 6$ mm was used. To ensure good statistics for the number of counts in the diffraction peaks, a typical measurement time of 1800 s was selected. A Gaussian function single peak fitting was used to determine the lattice spacing.¹⁶

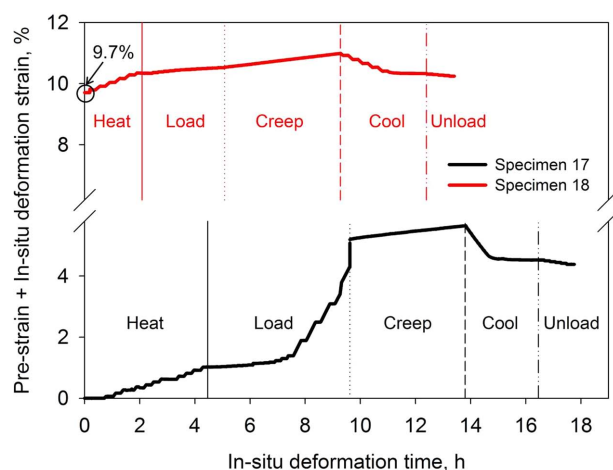
High temperature *in situ* neutron diffraction

Because each high temperature pre-strained specimen was unloaded at room temperature, followed by the *ex situ* neutron diffraction measurements of the internal misfit strains associated with the pre-strain, it has been inherently assumed that the internal misfit strain would not have redistributed or relaxed because of the cooling and unloading steps. To validate this assumption, specimens 17 and 18 (Table 2) were selected to undertake high temperature *in situ* neutron diffraction studies at ENGIN-X. The macroscopic strain of the bulk specimen was measured using a high temperature extensometer. Specimen 17 was not subjected to any pre-strain, while specimen 18 was creep pre-strained to a secondary creep state. These two specimens were subjected to *in situ* neutron diffraction studies, including (a) heating to 550°C, (b) loading to an engineering stress of 250 MPa; (c) creep for 4 h, (d) cool and finally and (e) unload at room temperature (Fig. 1). These sequential steps represent those incurred by the creep pre-strained specimens listed in Table 2. A typical measurement time of 600 s was selected together with a gauge volume of $3 \times 3 \times 4$ mm to ensure good counting statistics for the

Table 2 Summary of specimens subjected to high temperature pre-strain and the neutron diffraction source used for the measurements

Specimen ID	Material ID and microstructural condition	Pre-strain state (550°C)	Total inelastic strain (plastic + creep)		Neutron source	
			Plastic	Creep	ENGIN-X	POLDI
1, 2 and 3	H1 (EXLA)	No pre-strain	N/A	N/A	1 and 2	3
4 and 5		Loaded	1.9% and 1.8%	N/A	4	5
6 and 7		Primary creep	2.0% and 2.0%	0.9% and 1.2%	6	7
8–12		Secondary creep	2.0%, 2.2%, 2.3%, 2.4% and 2.7%	4.9%, 7.5%, 4.5%, 4.5% and 5.8%	8 and 9	10, 11 and 12
13	H1 (SA)	No pre-strain	N/A	N/A	13	
14		Loaded	5.9%	N/A	14	
15		Primary creep	5.1%	0.3%	15	
16		Secondary creep	5.8%	1.3%	16	
17	H1 (EXLA)	No pre-strain	0%		17	
18		Secondary creep	9.7%		18	

Specimens 4, 5 and 14 were loaded at 550°C to an engineering stress of 250 MPa. Specimens 6–12, 15–16 and 18 were loaded at 550°C to an engineering stress of 250 MPa and crept at the same engineering stress and temperature. All the abbreviations for describing material ID and microstructural condition can be found in 'Material for creep tests' and 'Material for oxidation tests' sections.



1 The macroscopic strain of specimens 17 and 18 accumulated during *in situ* high temperature deformation combined with neutron diffraction measurements. The origin of strain data for specimen 18 is at 9.7% to reflect the inelastic strain induced by pre-strain at 550°C. These two specimens were subjected to *in situ* neutron diffraction studies, including *a* heating to 550°C, *b* loading to an engineering stress of 250 MPa, *c* creep for 4 h, *d* cool and finally and *e* unload at room temperature

diffraction peaks. During the heating and cooling steps (a) and (d), measurements were undertaken by holding the temperature. During the loading step (b), measurements were undertaken using stress control for the elastic region and strain control for the plastic region. During the creep step (c), measurements were undertaken at intervals of 600 s. Finally during the unloading step (e), the specimen was held at several constant values of stress for the period of measurements.

Oxidation

Thermally aged 12 mm diameter cylinders were extracted from the EX header material (Table 1). Each specimen with a 12 mm diameter and a 7 mm height was polished to a colloidal silica oxide suspension (OPS) surface finish. This applies for specimens 19–23 in Table 3. The OPS surface finish was chosen for evaluating the oxidation rate, because it produced a deformation-free surface.^{12,17} In

Table 3 Summary of specimens exposed to a 1% CO/CO₂ gas environment oxidation at 550°C for a range of durations

Specimen ID	Material ID and microstructural condition	Oxidation time in 1% CO/CO ₂ at 550°C/h
19	H2 (EX)	0 (no oxidation)
20		10
21		100
22		500
23		1000
24	T (SA)	0 (no oxidation)
25		10
26		100
27		500
28		1000

All the abbreviations for describing material ID and microstructural condition can be found in 'Material for creep tests' and 'Material for oxidation tests' sections. Note: Specimen numbers were continued from the creep specimens given in Table 2.

fact, it has been shown that by removing the superficial cold worked Beilby layer, it is possible to study the true oxidation behaviour of the material^{18,19} as well as the fracture/environment interactions.^{19,20} Furthermore, an OPS polished surface promotes the formation of thick duplex oxide layers on Type 316H stainless steel.⁷ Solution annealed specimens for the oxidation tests were sliced from the stainless steel tube, specimens 24–28 in Table 3. Each specimen with a segmented circular shape had a typical height of 7 mm and a thickness of 4 mm. The detailed dimensions of the oxidation specimens (SA condition) have been given by Chen *et al.*⁷ One of the surfaces of these SA specimens prepared to an OPS surface finish was used for evaluating the oxidation rate and this provided a comparison with results from the EX specimens.

The oxidation tests were carried out in a horizontal double-walled quartz reaction tube. The controlled hot zone (150 mm length) temperature was within $\pm 1^\circ\text{C}$ of the set temperature of 550°C. Pure CO and CO₂ gases were mixed using calibrated digital flow metres to a fixed proportion of 1% CO/CO₂. The mixed gas was injected into the outer wall of the reaction tube where it was pre-heated, and then flowed into the inner wall of the reaction tube where the specimens were placed and oxidised. Full details of the oxidation reaction system have been given elsewhere by Chen *et al.*⁷

Oxidation tests were undertaken at a temperature of 550°C in a 1% CO/CO₂ gas environment for exposure times of 0, 10, 100, 500 and 1000 h at 1 atm (Table 3). The oxygen partial pressure for this gas environment was calculated to be 1.62×10^{-23} atm.⁷ and this is greater than that required to form magnetite (Fe₃O₄) but below that required to form haematite (Fe₂O₃). The content of 1% CO is typical of that found in the AGR pressure circuit coolant gas (from 0.6% to 1.2% CO).²¹

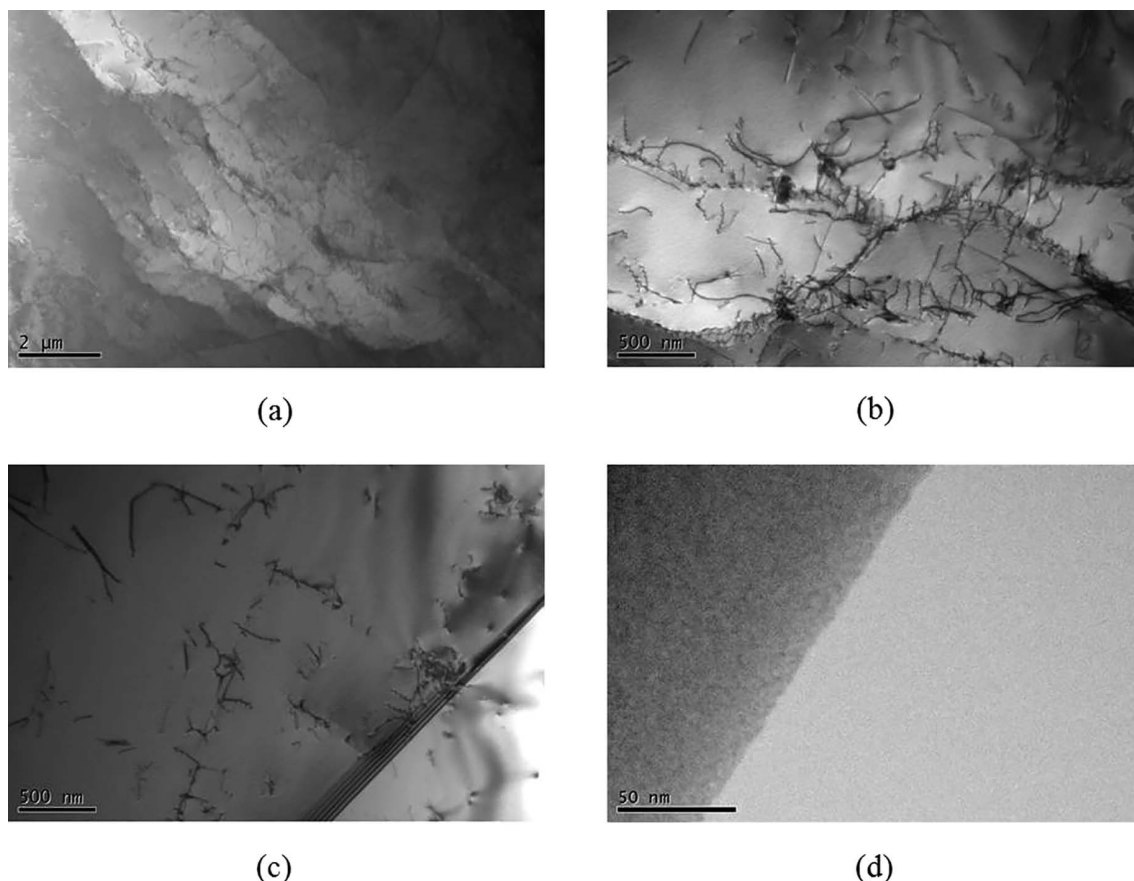
Post-oxidation characterisation

After the oxidation tests, specimens were removed from the reaction tube and together with the non-oxidised specimens were examined by optical microscopy. The oxidised and non-oxidised specimens (Table 3) were sectioned mechanically for evaluating the oxidation rate by measuring the thickness of oxides formed on the originally OPS polished surfaces. The cross-sectional surface of each specimen was prepared metallographically to an OPS surface finish and examined using both an optical microscope and a FEI Quanta 200 SEM. A backscattered electron detector fitted in the SEM was mainly used to enhance both the topographic and compositional contrast of the images. Both the outer and inner oxide thicknesses were measured and at least 20 SEM images with a magnification of $1000\times$ were analysed for each specimen.

Results

Effect of thermal aging on microstructure

The TEM observation of dislocation structures was carried out on both EX and SA Type 316H stainless steel specimens. The presence of the dislocation sub-grain structure was observed in the EX specimen (Fig. 2a). This is consistent with the typical dislocation structure for the material, which was subjected to high temperature creep.²² In addition, the presence of intra-granular precipitates was found in the EX specimen (Fig. 2b). A higher number of dislocations are present in the EX specimen



a EX specimen showing the presence of high temperature creep associated sub-grain structure; **b** EX specimen showing the presence of intra-granular precipitates and their interaction with dislocations; **c** SA specimen showing a grain boundary where the presence of the isolated dislocation can be seen for the grain on the left hand side; **d** SA specimen showing a grain boundary free of inter-granular precipitates

2 Transition electron microscopic images of both EX and SA Type 316H stainless steel specimens

(Fig. 2b), when compared with that in the SA specimen (Fig. 2c). The grain boundary of the SA specimen is observed to be free of inter-granular precipitates (Fig. 2d). The thicker areas of the TEM thin foils were then examined by using SEM to reveal the microstructure information at a lower magnification for both EX and SA specimens. Figure 3a shows the microstructure of the EX specimen, where the presence of both the inter-granular and intra-granular second-phase precipitates is confirmed. In contrast, the grain boundaries of the SA specimen are almost free of precipitates, although some pull-out holes can be observed in Figure 3b. In addition, the number of intra-granular precipitates in EX specimen is much higher than that in the SA specimen (Fig. 3a and b). From both the TEM and SEM images (Figs. 2 and 3), it is clear that the service history of the plant has an influence on the microstructure of Type 316H austenitic stainless steel.

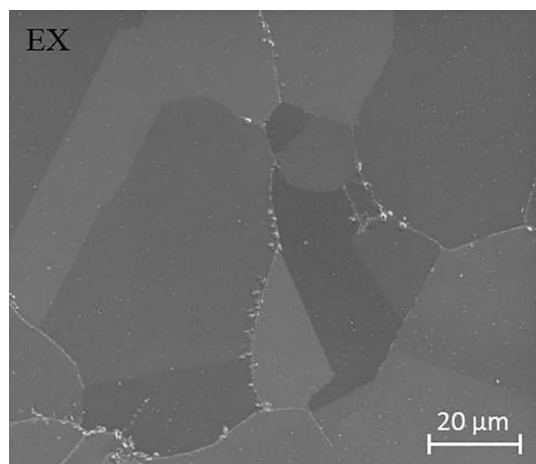
Effect of thermal aging on creep rate

Uniaxial creep tests were undertaken by using two Type 316H stainless steels with different microstructures: (i) EXLA and (ii) SA. Both EXLA and SA creep specimens were deformed at 550°C and at a range of tensile stresses from 250 to 320 MPa, as described in 'Creep' section. Figure 4 shows the steady state true creep rate for these two conditions and EX Type 316H stainless steel creep data are included in Figure 4 for comparison. The latter data for

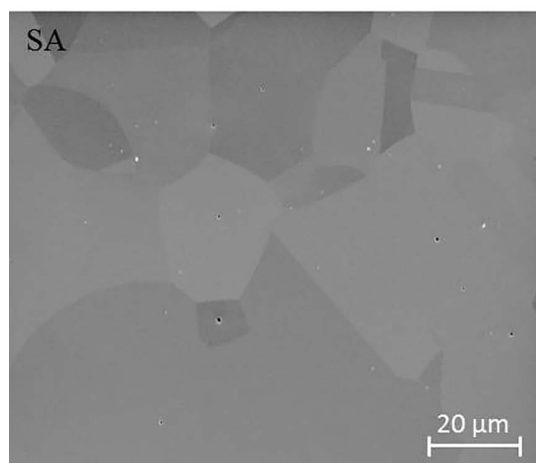
EX specimens²³ were obtained from a range of EX AGR superheater headers. They were subjected to plant service for between 51,000 and 68,700 h at temperatures between 490 and 530°C.²³ Creep rates for EXLA specimens were found to be the highest among the three microstructural conditions with a creep stress exponent of $n = 10.8$. Good reproducibility was found between the replicate tests conducted at an engineering stress of 250 MPa (Fig. 4). Creep data for the SA specimens showed the lowest creep rate with a creep stress exponent of $n = 4.6$, which was much smaller than that determined for both the EXLA and EX specimens (Fig. 4).

Internal misfit strains between grains induced by high temperature pre-strain

As described in 'Room temperature *ex situ* neutron diffraction' section, EXLA specimens 4–12 and SA specimens 14–16 were subjected to tensile pre-strain at 550°C. The plastic and creep pre-strains for each specimen are summarised in Table 2. The total inelastic strain for each specimen can be calculated by summing these two. The macroscopic stress-strain relationships for each specimen that include both the loading and creep states can be found in Refs. 5 and 13. The internal misfit strains between grains, measured along the axial direction of each specimen by neutron diffraction, are summarised in Figure 5 for the four grain families {111}, {200}, {220} and {311} as a function of the accumulated



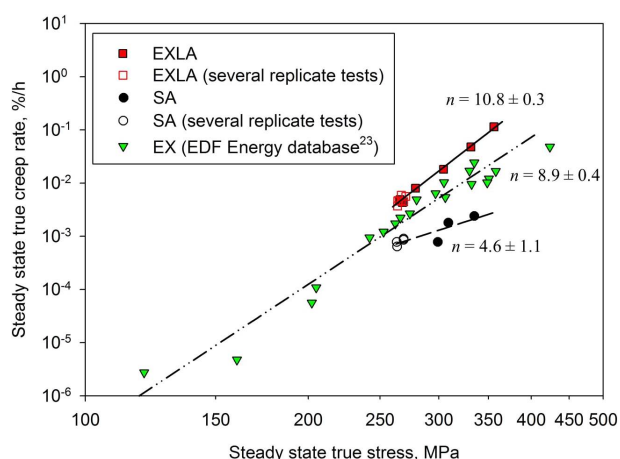
(a)



(b)

a EX specimen that was subjected to a plant service; b SA specimen that was subjected to a solution annealing heat treatment

3 Scanning electron microscopic images showing the effect of thermal aging on the microstructure of Type 316H austenitic stainless steel

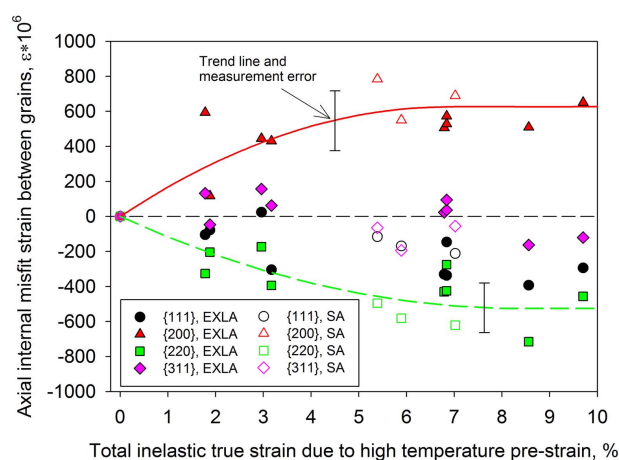


4 The steady state true creep rate v. the applied steady state true stress obtained from uniaxial creep tests on Type 316H stainless steels with different microstructural conditions. EXLA: EX plus laboratory aged condition; SA: solution annealed condition; EX: ex-service condition. EX creep data were obtained from Ref. 23

inelastic pre-strain at 550°C. These misfit strains for the $\{200\}$ grain family were tensile, whereas for both the $\{220\}$ and $\{111\}$ grain families they were compressive (Fig. 5). The measurement error indicated in Figure 5 represents that caused by the variation in the measured stress-free lattice spacings from specimens 1 and 2 in Table 2. The misfit strains for the $\{311\}$ grain family were the smallest among all four grain families. In addition, there was no significant difference between the EXLA and SA specimens in terms of the dependence of the misfit strains on the inelastic strain; see the trend lines in Figure 5. Clearly the misfit strains tended to approach limiting values when the specimen was subjected to inelastic strains greater than 7% (Fig. 5). An attempt was made to correlate the neutron diffraction measured internal misfit strains with either the plastic pre-strain or the creep pre-strain. It was found that the internal misfit strains were dependent on the level of the creep strain for each specimen. This does not necessarily indicate that the internal misfit strains were independent of the plastic strain associated with each specimen. Because all the pre-strained specimens were initially loaded to the same engineering stress, a similar amount of plastic strain was introduced to each specimen (see Table 2). For the EXLA specimens, the plastic strain ranges from 1.8% to 2.7%, and for the SA specimens, this strain ranges from 5.1% to 5.9% (Table 2). In ‘Validation of room temperature neutron diffraction experimental approach’ section, we will explore the effect of plastic strain on the creation of internal misfit strains.

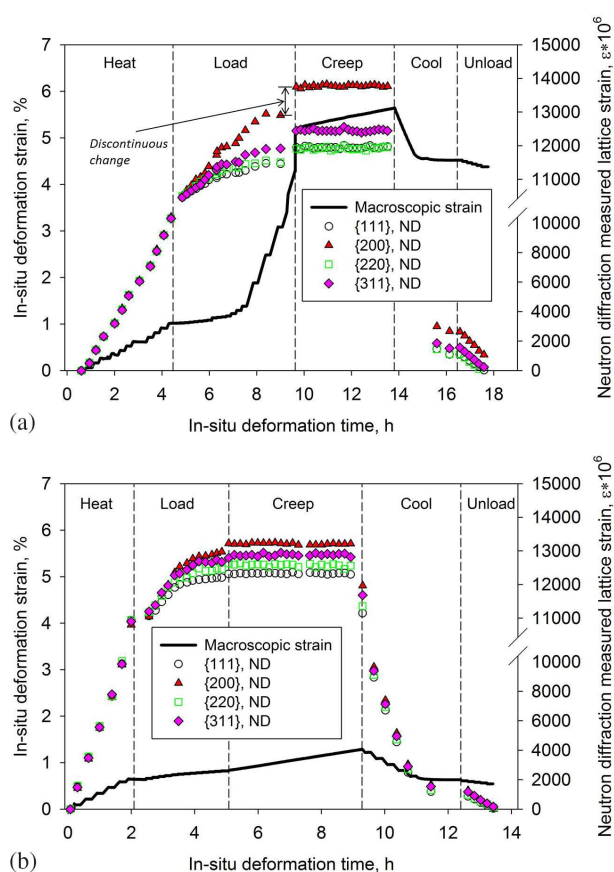
Validation of room temperature neutron diffraction experimental approach

As described in ‘High temperature *in situ* neutron diffraction’ section, there is a need to validate the assumption that the internal misfit strain did not redistribute or relax during the cooling and unloading steps for those pre-strained specimens. This is essential to evaluate the internal misfit strains in ‘Room temperature *ex situ* neutron diffraction’ and ‘Internal misfit strains between grains induced by high temperature pre-strain’ sections.



5 Axial internal misfit strains between grains because of high temperature pre-strains of both EXLA (EX plus laboratory aged condition) and SA (solution annealed) specimens summarised in Table 2

The EXLA specimens 17 and 18 were subjected to *in situ* neutron diffraction combined with creep deformation at 550°C (Fig. 1). Non-pre-strained specimen 17 and secondary creep pre-strained specimen 18 (Table 2) were first heated to 550°C (see Fig. 1). Lattice strains, measured for all four grain families, increased linearly as the temperature increased; this applies to specimens 17 and 18 (Fig. 6a and b). During the load step, the non-pre-strained specimen 17 showed the presence of incompatible misfit strains among the four grain families, where the lattice strain measured for the {200} grain family increased much faster than the other three, indicating the generation of internal misfit strains (Fig. 6a). The secondary creep pre-strained specimen 18 showed no incompatible strains during loading (Fig. 6b). During the creep step, there were constant lattice strains for both specimens 17 and 18 (Fig. 6a and b). This indicates that no internal misfit strains were generated during creep of 4 h. The discontinuous change from the loading to the creep steps observed in specimen 17 shown in Figure 6a was caused by the programming to change the loading mode. After the specimens were cooled to room temperature, they were finally unloaded at room temperature (Fig. 6a and b). The non-pre-strained specimen 17 showed the presence of residual lattice strains, in particular for the {200} grain family ($\epsilon_{200} = 1085 \times 10^{-6}$) in Figure 6a. This is consistent with the observed incompatible strains in the load step (Fig. 6a).



a Non-pre-strained EXLA specimen 17 and b secondary creep pre-strained EXLA specimen 18

6 Macroscopic strain together with the neutron diffraction measured lattice strains during *in situ* high temperature deformation combined with the neutron diffraction measurements

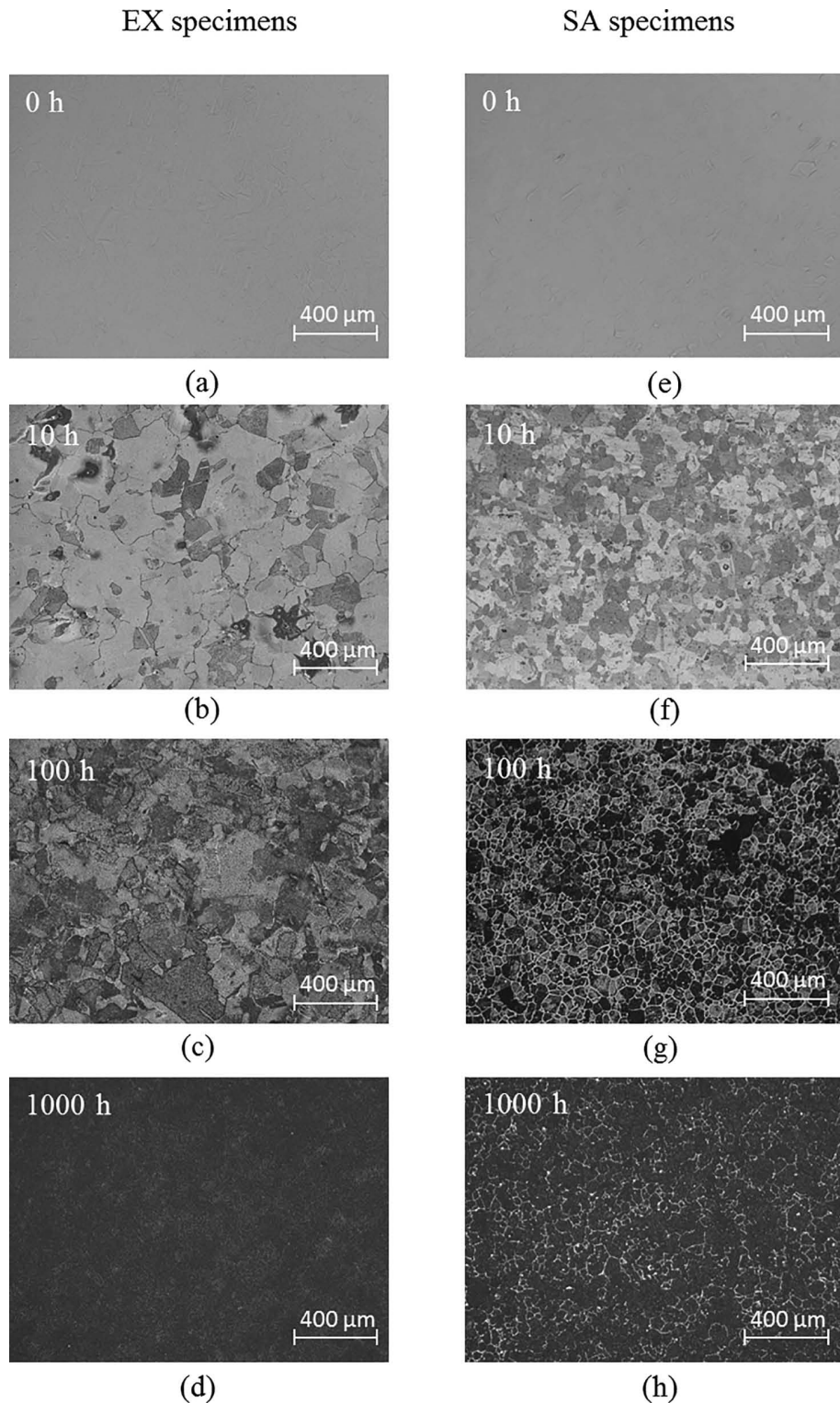
However, the secondary creep pre-strained specimen 18 showed approximately zero lattice strains for all four grain families when it was unloaded; no internal misfit strains were present in specimen 18.

Three important findings were revealed from this *in situ* neutron diffraction study. First, the presence of non-zero lattice strain at the final unloaded step of specimen 17 indicates that neutron diffraction can be used to measure the internal misfit strains, if the high temperature deformation introduces such an incompatible strain (Fig. 6a). Second, this type of internal misfit strain can be reliably measured using *ex situ* neutron diffraction, because there was no change of misfit strain when the pre-strained specimen 18 was loaded to produce a further secondary creep deformation; an approximate zero lattice strain ($\epsilon_{200} = 11 \times 10^{-6}$) was observed for the final unloaded step of specimen 18 (Fig. 6b). Therefore, the internal misfit strains measured by *ex situ* neutron diffraction for EXLA specimens 4–12 and SA specimens 14–16, as shown in Figure 5, provide a genuine measure of the misfit strain state associated with the pre-strain at 550°C. Third, the gradual increase in the measured lattice strains for the load step of Figure 6a indicate that the creation of internal misfit strains in this polycrystalline material is dependent on the accumulated incompatible strains. Thus the abrupt increase of the internal misfit strains as revealed in Figure 5 was because of the plastic strain introduced by loading the specimen to an engineering stress of 250 MPa. This will be discussed further in 'Model predictions of internal misfit strains' section via a multi-scale self-consistent model.

Effect of thermal ageing on oxidation

Figure 7 shows the progressive oxidation of the OPS polished surfaces for both the EX and SA specimens. Specimens were exposed at 550°C for different durations: 0, 10, 100 and 1000 h (see Table 3). Non-oxidised EX specimen 19 and SA specimen 24 (Fig. 7a and e) showed a mild topographical etch typical of an OPS surface finish. After 10 h oxidation, the larger grain size of the EX specimen 20 compared with the SA specimen 25 is revealed in Figure 7b and f. After 100 h oxidation, SA specimen 26 showed that oxides formed preferentially on the surface of the grains, but not along the grain boundaries as shown by the dark and bright contrasts in Figure 7g. Conversely, EX specimens did not show this type of contrast in Figure 7c; both the surfaces of grain and grain boundaries were oxidised after 100 h. After 1000 h oxidation, EX specimen 23 showed a heavily oxidised surface (Fig. 7d), whereas SA specimen 28 oxidised for 1000 h still revealed grain boundaries (Fig. 7h). This suggests that SA specimen 28 had different oxidation rates for the grain boundaries and grain surfaces. Specimens 22 (EX) and 27 (SA), oxidised for 500 h, are not shown here but followed the same trends.

Figure 8 shows the SEM cross-sectional views of oxidised EX specimen 23 and SA specimen 28. Both specimens were oxidised at 550°C for 1000 h in a 1% CO/CO₂ environment. The presence of duplex oxide layers, which consist of outer and inner oxides, can be seen for both specimens, Figure 8a for EX specimen 23 and Figure 8b for SA specimen 28. The oxide grew preferentially along the grain boundaries for EX specimen 23, leading to significant inter-granular oxide penetration (Fig. 8a). It should be noted that the grain

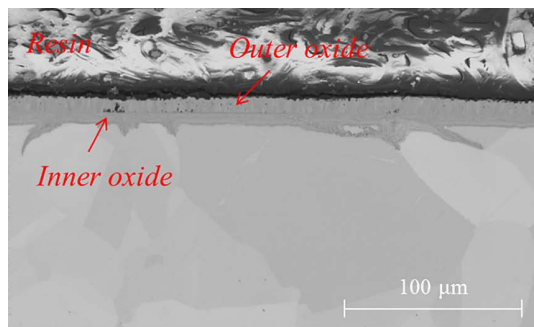


a Non-oxidised EX specimen 19; *b* EX specimen 20 oxidised for 10 h; *c* EX specimen 21 oxidised for 100 h; *d* EX specimen 23 oxidised for 1000 h; *e* non-oxidised SA specimen 24; *f* SA specimen 25 oxidised for 10 h; *g* SA specimen 26 oxidised for 100 h; *h* specimen 28 oxidised for 1000 h

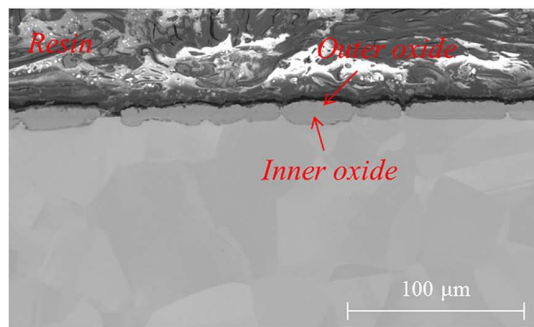
7 Optical micrographs of oxidised specimens subjected to a 1% CO/CO₂ environment at 550°C for different time durations

structures in Figure 8*a* and *b* were revealed by using backscattered electron imaging combined with OPS polishing as described in 'Post-oxidation characterisation' section. For SA specimen 28, the presence of thick duplex oxide layers can be seen within the grains, but less oxide formed at grain boundaries (Fig. 8*b*). Higher magnification SEM images revealed inter-granular oxide

penetration in the EX specimen 23 (Fig. 9*a*). Moreover crystallographic features of the outer oxide as well as the multi-layered structure of the inner oxide can be seen in Figure 9*a*. The latter is associated with the heterogeneously distributed Ni.⁷ SA specimen 28 showed no inter-granular oxide penetration (Fig. 9*b*), although the duplex oxide layers were also present for the grains.



(a)



(b)

a Specimen 23 in the thermally aged microstructural condition; **b** specimen 28 in the solution annealed microstructural condition. Note: the specimens were cross-sectioned to reveal sub-surface information

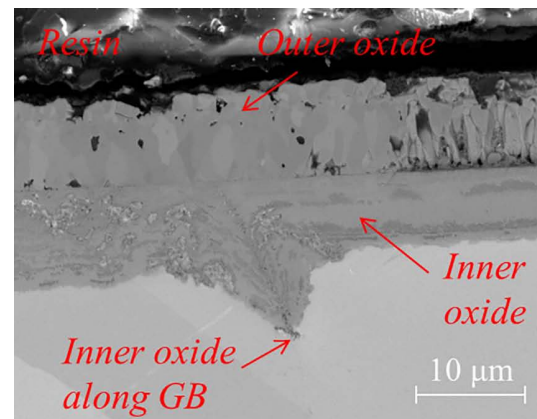
8 Backscattered electron images of oxidised specimens subjected to a 1% CO/CO₂ environment at 550°C for 1000 h

Finally, the oxide thickness for EX specimen 23 was much greater than that for SA specimen 28; this applies for both the outer and the inner oxides (Fig. 9a and b).

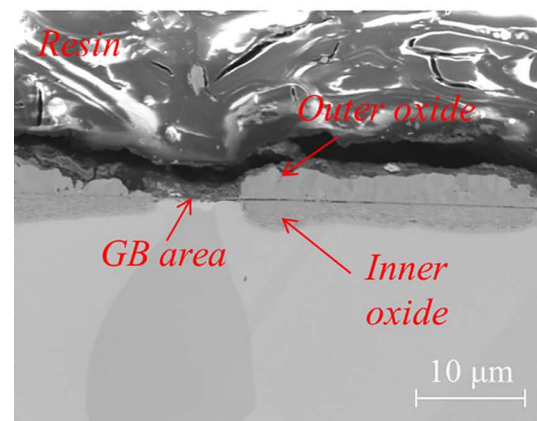
The oxide thickness was measured for the cross-sectional specimens 19–23 (EX material) and 24–28 (SA material). The measurements were carried out on both the optical images and SEM images using ImageJ software. Figure 10a compares the measured total oxide thickness for EX and SA specimens; optical and SEM data are in good agreement. EX specimens had a thicker oxide than the SA specimens, as shown in Figure 10a. The difference in thickness between these two conditions increased at the longer oxidation time. The higher values of standard deviation (STDEV) for the measured results of EX specimens reflect the effect of the inter-granular oxide penetration, as revealed in Figures 8a and 9a. The inner oxide thicknesses y (μm) for both EX and SA specimens are shown in Figure 10b together with the best fits by using a parabolic law²⁴

$$y^2 = k_p x \quad (2)$$

where x is the oxidation time in h and k_p is the parabolic rate law constant in μm²/h. A parabolic rate constant $k_p = 0.074$ μm²/h was determined for EX specimens and $k_p = 0.014$ μm²/h for SA specimens. The parabolic oxide growth law provided a reasonable fit to the measured oxide thickness (Fig. 10b).



(a)



(b)

a Specimen 23 with thermally aged microstructural condition showing the preferential inner oxide growth along a grain boundary (GB), **b** specimen 28 with solution annealed microstructural condition showing the absence of inner oxide in the area of GB

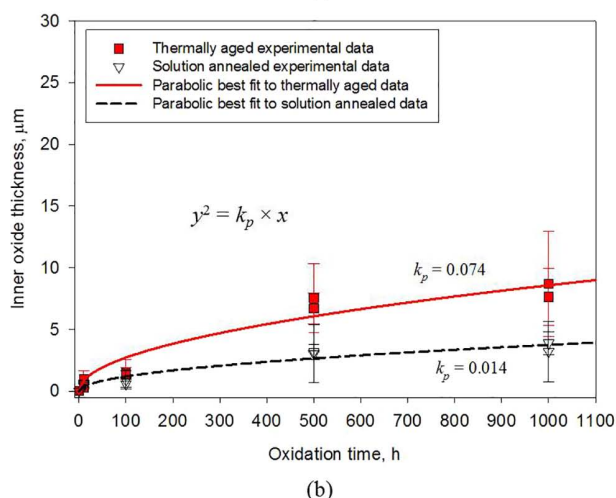
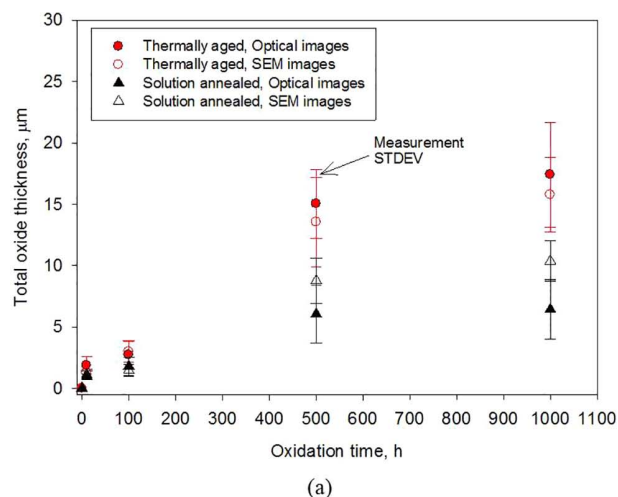
9 Backscattered electron, higher magnification images of oxidised specimens created in a 1% CO/CO₂ environment at 550°C for 1000 h

Discussion

Effect of microstructure on creep and oxidation

Certainly, changes in the microstructure of Type 316H stainless steels over the service history modify both creep deformation rate (Fig. 4) and oxidation rate (Fig. 10). It has been revealed by examination of the microstructure that EX material contains a higher number of both intra-granular and inter-granular second-phase precipitates compared with SA material (Fig. 3a and b). Both the dislocation density and arrangement are different for the EX and SA materials (Fig. 2a and c). There is of course an interaction between the thermal aging and the creep deformation, both with respect to the kinetics of the precipitation and the rate of creep deformation.²⁵

In terms of creep deformation, a higher number of second-phase precipitates, such as M₂₃C₆ carbides, lead to a decrease in the concentration of solute elements for the austenitic matrix. This will modify the rate of creep deformation because of the change in the magnitude of resistance to dislocation motion.²⁶ The highest creep rate for the EXLA material in Figure 4 suggests that the



a Total oxide thickness and **b** inner oxide thickness for both thermally aged and solution annealed microstructural conditions. A parabolic law was used to provide the best fits to the measured inner oxide thickness

10 Measurements of oxide thickness based on both optical micrographs and SEM micrographs of cross-sectional oxidised specimens subjected to a 1% CO/CO₂ environment at 550°C for 0, 10, 100, 500 and 1000 h

resistance to dislocation motion decreases with the presence of carbide precipitates developed over the service history. In addition, the lowest creep rate for the SA material in Figure 4 indicates that the resistance to dislocation motion increases with the increasing concentration of solid solution elements. Creep degradation, because of creep cavitation, is likely to increase as the inter-granular precipitates facilitate cavity nucleation.²⁷ This could also lead to the increase in the creep rate. However, this is not the main reason for the observed increase in creep rate for the EXLA material (Fig. 4) because true creep rates were determined from the steady state (secondary creep) rather than the tertiary creep stage.

In terms of oxidation, the presence of second-phase precipitates changes the chemical composition at grain boundaries, which leads to inter-granular oxide penetration, Figure 8a and b for EX and SA materials, respectively. The grain boundaries of SA material do not contain any second-phase precipitates (Fig. 3b), and therefore, have not been depleted in oxidation-protective

elements, such as chromium. However, progressive thermal aging leading to the presence of second-phase precipitates at grain boundaries (Fig. 3a) will reduce their oxidation resistance. In addition, the presence of intra-granular second-phase precipitates is shown in Figure 3a, which could account for the overall higher oxidation rate in EX material when compared with SA material (Fig. 10).

Model predictions of internal misfit strains

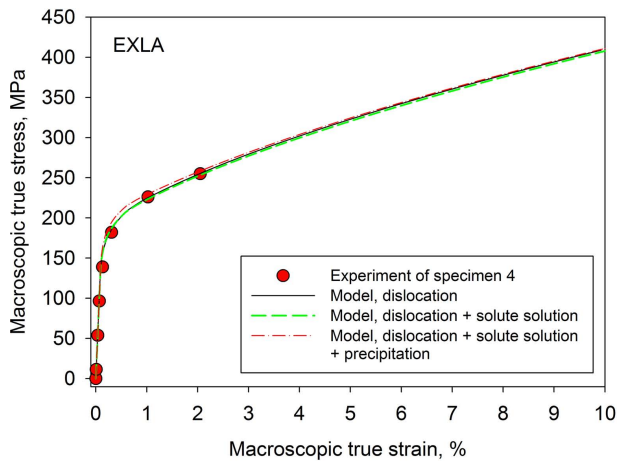
A multi-scale self-consistent model

The magnitude of internal misfit strains between grains is a function of the total inelastic strain introduced by high temperature pre-straining (Fig. 5). It has been demonstrated by previous work^{5,13,28} that a multi-scale self-consistent model can provide detailed information about the evolution of internal misfit strain/stress in the individual grains of a polycrystal. The model consists of three sub-models: (i) continuum, (ii) crystal plasticity and (iii) dislocation link-length, where the last of these is based on a model originally proposed by Lagneborg and Forsen.²⁹ However, this has been extended to describe interactions between dislocations and other microstructural features, such as forest dislocation junctions, solute atoms and second-phase precipitates; each dependent on the thermal aging condition of the Type 316H stainless steel. Note that the SA material involves only dislocation and solute strengthening, whereas all three strengthening contributions are present in the EXLA material. Research on the effects of creep recovery of the dislocation structures is continuing, thus our consideration is limited to elastic and plastic deformation. Details of the model can be found elsewhere.^{30,31}

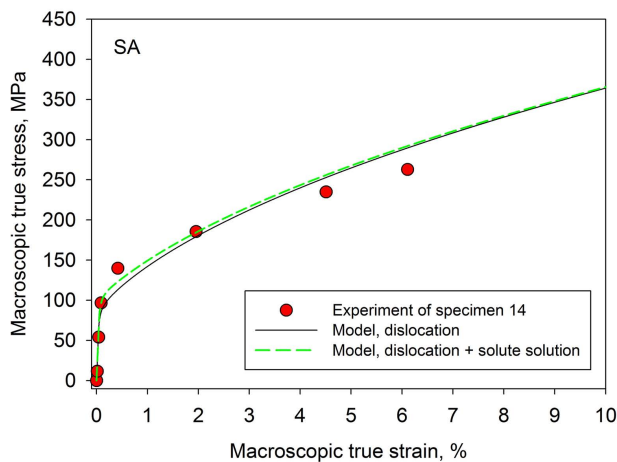
The development of internal misfit strain/stress within each grain is determined by the accumulated incompatible inelastic mismatch strains that develop between the grain and the surrounding matrix. The inelastic strain increments within each grain are calculated using a crystal plasticity framework by adding contributions from all active slip systems within the grain. This is formulated by a rate-dependent power-law such that dislocation slip occurs on a single system when the resolved shear stress approaches the material internal resistance. Material internal resistance describes the critical resolved shear strength (CRSS) required for a dislocation to propagate on the slip plane, as described by Chen *et al.*¹⁰ The magnitude of this term depends on the dislocation interactions with other dislocations and other types of obstacles (sub-model iii). Because the thermal aging has been demonstrated to change the microstructure of Type 316H stainless steel as revealed in Figures 2 and 3, it is instructive to provide a physical description for the magnitude of the material internal resistance.

Effect of thermal aging on material internal resistance

The model is used to fit the macroscopic stress–strain response of SA specimen 14 and EXLA specimen 4 tested at 550°C. The fitted macroscopic stress–strain curves compared with the experimental data are shown in Figure 11. The best fits to the macroscopic stress–



(a)



(b)

11 Comparison of the experimentally obtained macroscopic stress-strain curves with the model predictions for a EXLA specimen 4 and b SA specimen 14. Note: the predicted macroscopic stress-strain relationship was given up to 10% (covering those reported in Table 2) although the experimental loading curve provided a 2% strain for EXLA specimen 4 and a 6% strain for SA specimen 14.

strain response in Figure 11 were achieved by the use of material internal resistance of 61.5 MPa for EXLA specimen 4 and 31.1 MPa for SA specimen 14. This is the same order of difference for the macroscopic initial yield strengths between the two microstructural conditions. Now the formulation of the material internal resistance is considered in the context of different types of dislocation interactions.

The dislocation link-length model describes a two-dimensional distribution of forest dislocation links on slip planes of individual grains, which is related to dislocation pinning points. The model illustrates the strengthening effect of the dislocation-to-dislocation interactions where the CRSS on each slip plane is inversely proportional to the mean spacing of the pinning points. The corresponding material internal resistance τ_{ir}^1 is given by

$$\tau_{ir}^1 = \frac{\alpha_1 Gb}{L_1} \quad (3)$$

where L_1 is the mean spacing of dislocation pinning points on the slip plane, G is the shear modulus at 550°C, b is the length of the Burgers vector and α_1 is a dimensionless constant describing the strength of the dislocation pinning points. For Type 316H stainless steels,

the values of G , b and α_1 have been reported in previous work^{4,32,33} and are summarised in Table 4. These material constants are assumed to be the same for both the EXLA and SA specimens. It is the difference in the magnitude of L_1 in Table 4 that leads to the different magnitude of material internal resistance for EXLA specimen 4 and SA specimen 14.

The effect of solid solution or precipitation on the resistance to slip (i.e. material internal resistance) is considered to be inversely proportional to the mean spacing of the randomly distributed solute atoms or the second-phase precipitates. Based on the approach described by Chen *et al.*,¹⁰ a linear superposition rule was adopted to determine the internal resistance associated with forest dislocations and solute atoms

$$\tau_{ir}^{1+2} = \frac{\alpha_1 Gb}{L_1} + \frac{\alpha_2 Gb}{L_2} \quad (4)$$

where α_2 describes the strength of the solute atoms contribution and depends on the difference in size between solute and matrix atoms.^{32,34} L_2 was derived from the number density of solute atoms³⁴ by using the chemical composition given in Table 1.

Dislocations by-passing precipitates by an Orowan bowing mechanism lead to the formation of secondary dislocation loops around precipitates.³³ These loops contribute to the dislocation strengthening and introduce a local microscale misfit internal stress between the matrix and precipitates. Dong *et al.*³⁵ adopted a geometric mean or quadratic rule to describe the material internal resistance arising from combined dislocation and precipitation strengthening. Therefore, the overall material internal resistance from the multiple types of obstacles can be written as

$$\tau_{ir}^{1+2+3} = \sqrt{\left(\frac{\alpha_1 Gb}{L_1}\right)^2 + \left(\frac{\alpha_3 Gb}{L_3}\right)^2} + \frac{\alpha_2 Gb}{L_2} \quad (5)$$

where α_3 describes the strength of precipitates with a value of 0.84 obtained from Ref. ³⁶. The mean spacing of the precipitates L_3 was calculated from the estimated volume fraction f_v and the average radius r of the precipitates³⁷

$$L_3 = r \sqrt{\frac{2\pi}{3f_v}} \quad (6)$$

values of $r = 60$ nm and $f_v = 0.005$ were the best estimates according to Refs. ^{38–40} for $M_{23}C_6$ type precipitates. The resulting number density of solute atoms was calculated to be small, and the solute and precipitation strengthening are simplified to be isotropic on all the slip planes.

The initial material internal resistance is assumed to be identical for all the slip planes in all the grains. But this develops differently as described by self- and latent hardening laws for each slip plane because of the evolution of the distribution of pinning points. Note that changes in precipitation and solid solution composition during high temperature aging under load are not considered in this work. Thus α_2 , α_3 , L_2 and L_3 are fixed (Table 4), while L_1 in equations (3)–(5) is the only fitting parameter to obtain the material internal resistance of 61.5 MPa for EXLA specimen 4 and 31.1 MPa for SA specimen 14.

Table 4 Fitting parameters used in the multi-scale self-consistent model to calculate the magnitude of internal resistance at 550°C (in MPa)

Parameters for model prediction	Ex-service plus laboratory thermally aged (EXLA)			Solution annealed (SA)	
	Dislocation	Dislocation + solid solution	Dislocation + solid solution + precipitation	Dislocation	Dislocation + solid solution
α_1	0.35	0.35	0.35	0.35	0.35
L_1^*/m	1.35×10^{-7}	2.50×10^{-7}	2.58×10^{-7}	2.67×10^{-7}	1.00×10^{-6}
α_2	N/A	4.6×10^{-4}	4.6×10^{-4}	N/A	4.6×10^{-4}
L_2/m		3.6×10^{-10}	3.6×10^{-10}		3.6×10^{-10}
α_3		N/A	0.84		N/A
L_3/m		N/A	1.02×10^{-6}		
G/MPa	92000				
b/m	2.58×10^{-10}				

*The value of L_1 was obtained by a best fit to the experimentally macroscopic stress-strain data. L_2 and L_3 are kept constant throughout the fitting process.

The origins of material internal resistance are dependent on the microstructure produced by thermal aging. For the EXLA and SA specimens, the significance of different microstructures is examined by fitting the macroscopic response with a reduced number of strengthening contributions (see Table 4). If the experimentally determined microstructural information (ideally quantitative) becomes available, one can then identify the balance between different dislocation interaction mechanisms. Such microstructural information is important when considering the transient response of the material during long term exposure at elevated temperature, where both the size and distribution of the second-phase precipitates and the concentration of alloy elements in solid solution will be significant for controlling dislocation motion and arrangement.^{41–43}

Model prediction of internal misfit strains

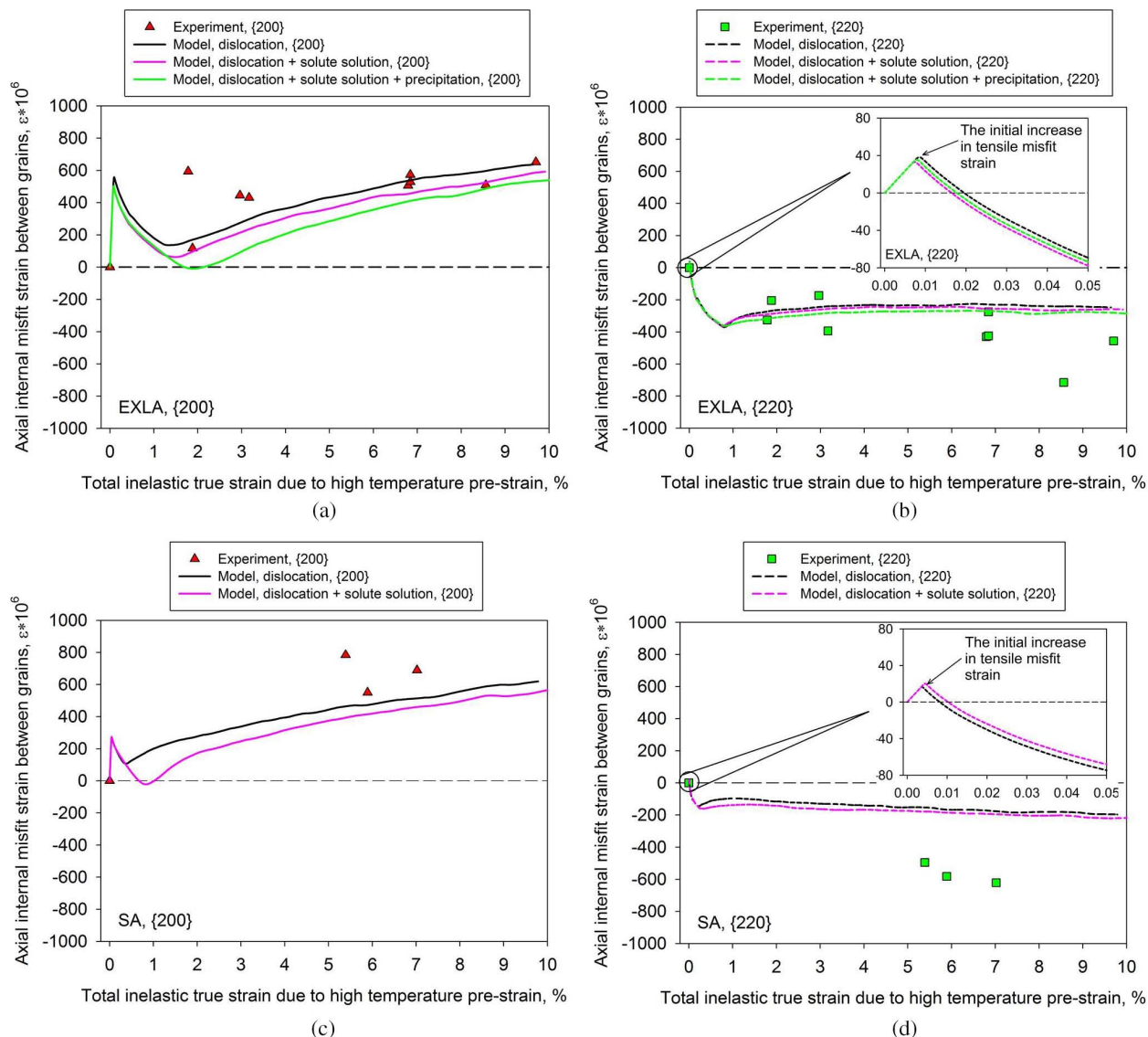
The self-consistent continuum scheme links the response of each individual grain with the macroscopic response of the polycrystalline aggregate.⁴⁴ Thus the evolution of the internal misfit strains for different grain families in EXLA specimen 4 and SA specimen 14 can be predicted by the multi-scale self-consistent model. Figure 12a–d compare the predictions with the measured internal misfit strains in terms of the {200} and {220} grain families for the EXLA and SA specimens. The predicted trends are similar for each specimen, with the internal strains for the EXLA specimen about a factor of two greater than those for the SA specimen; Figure 12a and b for EXLA specimen 4 and Figure 12c and d for SA specimen 14. This is the same order of difference for the material internal resistance between the two microstructural conditions. The small difference between the predictions of each model and the experimental data for a given specimen indicates that the creation of the internal misfit strains is dependent on the magnitude of the material internal resistance. In this case, the observed small difference between the predictions of each model is expected, because the magnitude of this material internal resistance was a constant value for each microstructural condition (61.5 MPa for EXLA specimen 4 and 31.1 MPa for SA specimen 14). Although a good agreement between model predictions and experiment can be found for EXLA specimen 4 (Fig. 12a and b), there is a less good agreement for SA specimen 14 (Fig. 12c and d). This indicates that the strengthening mechanisms considered in this study and the way in which they are

modelled may not necessarily capture the micro-mechanical response of the SA specimen. For example, solute atoms may not act as athermal obstacles, but are dragged by mobile dislocations at the temperatures and strain rates employed in the experiments.^{45,46} The detailed description about the evolution of internal misfit strains in Figure 12a–d is not extended here, because this is outside the main theme of this work.

Prediction of long term oxidation rate

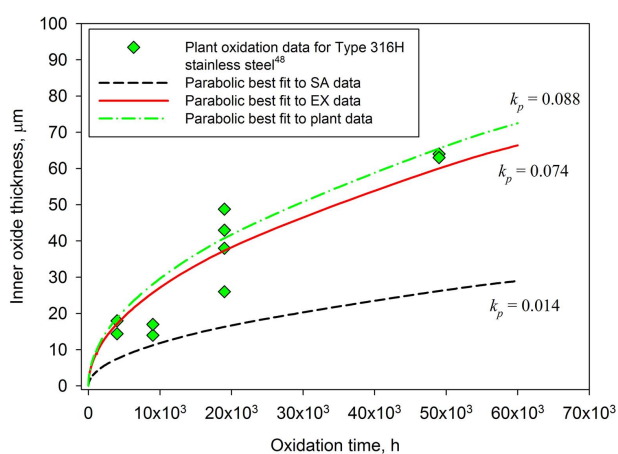
As shown in Figure 10b, inner oxide thickness can be fitted to a parabolic law for both the EX and SA materials. The parabolic law for the oxide growth suggests that the diffusion of ions, either metal or gas through the formed oxide layers, is the rate determining process.⁴⁷ By using curve fitting, the parabolic rate law constant k_p ($k_p = 0.074 \mu\text{m}^2/\text{h}$ for EX and $k_p = 0.014 \mu\text{m}^2/\text{h}$ for SA conditions respectively) was derived. This allows predictions of oxide thicknesses to be extrapolated to a much longer duration, about 60,000 h. These are compared with the AGR plant oxidation data⁴⁸ together with the curve fitting via a parabolic law with $k_p = 0.088 \mu\text{m}^2/\text{h}$ (see Fig. 13). The inner oxide thicknesses were reported in AGR plant oxidation data, rather than the total oxide thicknesses. This is because the outer oxides might spall from the component during service and when the component was removed and transported post-service. This would introduce uncertainties if the oxidation kinetics were established from the total oxide thicknesses. The derived rate constant of $k_p = 0.088 \mu\text{m}^2/\text{h}$ from plant oxidation data is similar to that derived from the short-term oxidation data based on EX specimens (Fig. 13). This indicates that the oxidation behaviour of an OPS surface finished Type 316H stainless steel is consistent with that observed on AGR plant developed over a service time of about 60,000 h. Furthermore, good agreement between the predicted EX oxidation rate and AGR plant oxidation rate demonstrates that microstructural changes arising from thermal aging play a key role in controlling oxidation rate over the plant service lifetime.

When comparing short-term laboratory based oxidation tests with long term plant oxidation exposure, it is important to bear in mind that the surface finishes of Type 316H stainless steels are unlikely to be the same. Type 316H stainless steels used in the AGR plant are almost certainly not deformation-free at the surface (i.e. not an OPS polished or electropolished), but more likely have received a



a {200} grain family of EXLA specimen 4; b {220} grain family of EXLA specimen 4; c {200} grain family of SA specimen 14; and d {220} grain family of SA specimen 14. The inserted figure is a magnified view of the initial increase in tension for the {220} grain family

- 12 Predicted internal misfit strains as a function of the inelastic strain introduced by the 550°C pre-strain, determined from self-consistent model. Results are compared with the neutron diffraction measurements



- 13 Comparison of the AGR plant oxidation data⁴⁸ and best fit curves with the two best fit curves derived from short-term oxidation tests on both SA and EX specimens

ground finish. By undertaking a short-term oxidation test of 500 h in a 1% CO/CO₂ environment at 550°C, it has been shown that a ground surface finish promotes the formation of a thin and protective oxide layer, $\leq 0.5 \mu\text{m}$ in thickness for Type 316H stainless steels.⁷ However, such a protective oxide layer must have degraded with time because EX Type 316H stainless steels, in general, form a thick duplex Fe-rich oxide of $\geq 15 \mu\text{m}$.⁴⁸ Although Type 316H stainless steel components before entering the plant service are subjected to a solution annealing heat treatment, the microstructure of the material progressively ages over the service lifetime. Thus the long term oxidation behaviour of Type 316H stainless steels can be predicted by undertaking short-term oxidation tests on OPS surface finished EX specimens, as shown in Figure 13.

Interaction between creep and oxidation

It is clear that the microstructures of Type 316H stainless steels change significantly with the service life.

Structural integrity assessments of components need to accommodate these changes in microstructures by allowing for the effects of both creep and oxidation. The discussion in 'Prediction of long term oxidation rate' section shows that the latter can be handled in a straightforward manner. The long term oxidation behaviour can be predicted from short-term tests on EX specimens with an OPS finish. Then the component response can be evaluated by reducing the component thickness by the thickness of metal loss associated with the oxide thickness. As oxide thicknesses are only about 0.1 mm at long times (Fig. 13), this effect is expected to be negligible in thick-section components (thicknesses > 10 mm) but more important in thinner section components, such as boiler tubes where thicknesses are only a few millimetres.

To allow for the long term creep response, Figure 4 shows that creep strain rates in EX material, which has been further laboratory aged (EXLA) are higher than those for SA material and material with only in service aging (EX). However, at lower stresses, which are more likely to be representative of service stresses, the trends in Figure 4 suggest that the data from the tests in the three material conditions may converge. This is, perhaps, not surprising as lower stress tests are associated with longer test durations and therefore automatically include some effects of thermal aging. Nevertheless, the EXLA data suggest that caution needs to be exercised in extrapolating short-term data for use in long term plant assessments.

Combining the suggestions in the last two paragraphs would imply that the effects of oxidation and thermal aging can be treated by allowing for metal loss and using appropriate thermally aged materials data. However, this assumes that the two mechanisms act independently and that the material response in the component is essentially homogeneous. However, this may not be the case as discussed by Biglari and Nikbin.⁴⁹ Those authors assume that creep and oxidation damage can be summed to give a total damage, which is high near the oxidising surface. In practice, it is unlikely that oxidation and creep damage can be simply summed, but it is possible that the oxidation affects the creep behaviour of the near-surface material. In this case, the component response is altered by the consequent non-homogeneous material response in addition to the thermal aging. In particular, the surface material response may be more brittle leading to failure being initiated by surface cracking rather than by bulk creep damage. This will depend on both the extent of the material affected near the surface and the ability of the bulk material to resist cracking by mechanisms such as creep. To address these mechanisms, high temperature fracture mechanics properties, as described by Webster and Ainsworth⁵⁰ for example, would be required in addition to the creep properties addressed in the present paper. Therefore, the oxidation and thermal aging data described here may not be sufficient to address component response if the failure mechanism changes from bulk creep damage to one dominated by near-surface local cracking.

Concluding remarks

The effects of the microstructural changes associated with the effects of thermal aging on material internal

state controls both the creep deformation and oxidation behaviour of Type 316H stainless steels. It is clear that the evolution of the microstructure over the service life of components exposed at temperatures between 470 and 530°C has a detrimental influence on both creep and oxidation resistance. For creep, it has been demonstrated that a multi-scale self-consistent model can predict reliably both the macroscopic response and each individual grain in a polycrystalline material, provided that the mechanisms of dislocation interaction with other dislocations and other obstacles are understood appropriately. For oxidation, a parabolic law obtained on short-term oxidation behaviour on an OPS surface finished thermally aged material can be used to predict the long term plant oxidation behaviour. Because the oxidation affects the creep behaviour of the near-surface material by altering the microstructure, there is a need to conduct an experimental study on their synergetic roles.

Acknowledgements

Bo Chen, Fabio Scenini and Robert Ainsworth are grateful for financial support from the ENVISINC project, which has been funded through Innovate UK (formerly Technology Strategy Board), part of UK Government Department for Business, Innovation and Skills. Additional funding to support this research was from EDF Energy Nuclear Generation Limited since 2011 when Bo Chen worked at University of Bristol as a research assistant. Bo Chen would like to thank Dr Timothy Joseph from University of Bristol for co-undertaking creep testing programme, Mr Ashokan Gopal from the University of Manchester for the measurements of oxide thickness. Last but not the least, thanks are given to Dr Shu Yan Zhang, Dr Saurabh Kabra from ENGIN-X beamline and Dr Steven Van Petegem from POLDI beamline for assisting with the neutron diffraction measurements. This paper is published with the permission of EDF Energy Nuclear Generation Ltd.

References

1. OECD: 'Challenges in long-term operation of nuclear power plants: implications for regulatory bodies'; Nuclear Regulation NEA/CNRA/R(2012)5, ISBN: 978-92-64-99187-3, Nuclear Energy Agency Organisation for Economic Co-operation and Development (OECD), France 2012.
2. Flewitt P. E. J.: 'Structural Integrity Assessment of High Integrity Structures and Components: User Experience'. 7th Int. Conf. on Mechanical Behaviour of Materials – ICM7, 143–163, The Hague, The Netherlands, 28th May – 2nd June 1995, Delft University Press.
3. Stoter L. P.: 'Thermal ageing effects in AISI type 316 stainless steel', *J. Mater. Sci.*, 1981, 16, 1039–1051.
4. Clausen B., Lorentzen T. and Leffers T.: 'Self-consistent modelling of the plastic deformation of FCC polycrystals and its implications for diffraction measurements of internal stresses', *Acta Mater.*, 1998, 46, 3087–3098.
5. Chen B., Hu J. N., Flewitt P. E. J., Smith D. J., Cocks A. C. F. and Zhang S. Y.: 'Quantifying internal stress and internal resistance associated with thermal ageing and creep in a polycrystalline material', *Acta Mater.*, 2014, 67, 207–219.
6. Daymond M. R. and Bouchard P. J.: 'Elastoplastic deformation of 316 stainless steel under tensile loading at elevated temperatures', *Metall. Mater. Trans. A*, 2006, 37, 1863–1873.
7. Chen B., Lindsay J., Ainsworth R. A. and Scenini F.: 'Oxidation behaviour of an austenitic stainless steel used in UK advanced gas cooled reactors'. Corrosion 2015, Dallas, USA, March 2015, NACE International.
8. O'Donnell M. P., Bradford R., Dean D. W., Hamm C. D. and Chevalier M.: 'High temperature issues in advanced gas cooled reactors (AGR)'.

- TAGSI/FESI Symposium: Structural Integrity of Nuclear Power Plant, The Welding Institute, Cambridge, 2013, EMAS Publishing.
9. Ainsworth R. A.: 'R5 procedures for assessing structural integrity of components under creep and creep-fatigue conditions', *Int. Mater. Rev.*, 2006, 51, 107–126.
 10. Chen B., Flewitt P. E. J., Cocks A. C. F. and Smith D. J.: 'A review of the changes of internal state related to high temperature creep of polycrystalline metals and alloys', *Int. Mater. Rev.*, 2015, 60, 1–29.
 11. Putatunda S. K.: 'Corrosion behaviour of sensitised austenitic (AISI 304) stainless steel in a CO₂ atmosphere', *Mater. Sci. Eng. A*, 1987, 91, 89–95.
 12. Chen B., Flewitt P. E. J. and Smith D. J.: 'Microstructural sensitivity of 316H austenitic stainless steel: residual stress relaxation and grain boundary fracture', *Mater. Sci. Eng. A*, 2010, 527, 7387–7399.
 13. Chen B., Hu J. N., Wang Y. Q., Zhang S. Y., Van Petegem S., Cocks A. C. F., Smith D. J. and Flewitt P. E. J.: 'Role of the misfit stress between grains on the Bauschinger effect for a polycrystalline material', *Acta Mater.*, 2015, 85, 229–242.
 14. Chen B., Hu J. N., Wang Y. Q., Kabra S., Cocks A. C. F., Smith D. J. and Flewitt P. E. J.: 'In-situ neutron diffraction study of the internal strains between grains during creep deformation', *J. Mater. Sci.*, 2014, [Under Review].
 15. Santisteban J. R., Daymond M. R., James J. A. and Edwards L.: 'ENGIN-X: a third-generation neutron strain scanner', *J. Appl. Cryst.*, 2006, 39, 812–825.
 16. Weisser M. A., Evans A. D., Van Petegem S., Holdsworth S. R. and Van Swygenhoven H.: 'In situ room temperature tensile deformation of a 1% CrMoV bainitic steel using synchrotron and neutron diffraction', *Acta Mater.*, 2011, 59, 4448–4457.
 17. Buehler: 'Oxide polishing', 2015; available at: <http://www.buehler.co.uk/products/consumables/oxide-polishing.html>.
 18. Newman R. C. and Scenini F.: 'Another way to think about the critical oxide volume fraction for the internal-to-external oxidation transition?', *Corrosion*, 2008, 64, 721–726.
 19. Scenini F., Newman R. C., Cottis R. A. and Jacko R. J.: 'Effect of surface preparation on intergranular stress corrosion cracking of alloy 600 in hydrogenated steam', *Corrosion*, 2008, 64, 824–835.
 20. Scenini F. and Sherry A. H.: 'SCC of sensitized 304SS in high temperature water with anionic impurities contamination', *Corrosion*, 2012, 68, 1094–1107.
 21. Smith N. M.: 'Summary of AGR Coolant Composition 2010', Report E/REP/BPKB/0093/AGR/11, EDF Energy Nuclear Generation Ltd. 2013, Barnwood, UK.
 22. Pahutova M., Cadek J. and Cerny V.: 'Transients in the creep of a 16Cr–12Ni–2.5Mo austenitic steel II: structure', *Mater. Sci. Eng.*, 1984, 62, 33–40.
 23. Spindler M. W.: 'The multiaxial creep ductility of ex-service Type 316H at 550°C', British Energy Report E/REP/ATEC/0020/AGR/01; 2001, Barnwood, UK.
 24. Chevalier S.: '1-07 – mechanisms and kinetics of oxidation', in 'Shreir's corrosion', (ed. Cottis B.), 135–136; 2010, Oxford, UK, Elsevier.
 25. Skelton R. P. and Horton C. A. P.: 'The effect of thermal ageing and mechanical exposure on low cycle creep-fatigue strength of 316 steel at 625°C', *Mater. High Temp.*, 1999, 16, 87–97.
 26. Friedel J.: 'Dislocations', 1964, London, Pergamon Press Ltd.
 27. Dyson B. F.: 'Continuous cavity nucleation and creep fracture', *Scripta Metall.*, 1983, 17, 31–37.
 28. Hu J. N., Chen B., Smith D. J., Flewitt P. E. J. and Cocks A. C. F.: 'Self-consistent modeling and the evaluation of lattice deformation in a polycrystalline austenitic stainless steel'. Joint 3rd UK-China Steel Research Forum & 15th CMA-UK Conf. Mater. Sci. Eng., ISIS, UK, 2014, Materials Today: Proceedings.
 29. Lagneborg R. and Forsen B. H.: 'A model based on dislocation distributions for work-hardening and the density of mobile and immobile dislocations during plastic flow', *Acta Metall.*, 1973, 21, 781–790.
 30. Hu J. N.: 'A theoretical study of creep deformation mechanisms of type 316H stainless steel at elevated temperatures', Department of Engineering Science, PhD, University of Oxford, Oxford; 2015.
 31. Hu J. N. and Cocks A. C. F.: 'A multi-scale self-consistent model describing the lattice deformation in austenitic stainless steel', *Int. J. Solids. Struct.*, 2015, [Submitted].
 32. Bhadeshia H. K. D.: 'Mechanical properties of steels 16: solid solution strengthening', Youtube through: <http://www.msm.cam.ac.uk/phase-trans; 2013>.
 33. Ashby M. F.: 'The theory of the critical shear stress and work hardening of dispersion-hardened crystals', 1966, UK, Defense Technical Information Center.
 34. Hirth J. P. and Lothe J.: 'Theory of dislocations', 1982, New York, John Wiley.
 35. Dong Y., Nogaret T. and Curtin W. A.: 'Scaling of dislocation strengthening by multiple obstacle types', *Metall. Mater. Trans. A*, 2010, 41, 1954–1960.
 36. Foreman A. J. E. and Makin M. J.: 'Dislocation movement through random arrays of obstacles', *Phil. Mag.*, 1966, 14, 911–924.
 37. Simar A., Brechet Y., de Meester B., Denquin A. and Pardoen T.: 'Sequential modeling of local precipitation, strength and strain hardening in friction stir welds of an aluminum alloy 6005A-T6', *Acta Mater.*, 2007, 55, 6133–6143.
 38. Chen B., Flewitt P. E. J., Smith D. J. and Jones C. P.: 'An improved method to identify grain boundary creep cavitation in 316H austenitic stainless steel', *Ultramicroscopy*, 2011, 111, 309–313.
 39. NIMS Creep Data Sheet: 'Metallographic atlas of long-term crept materials', 2013, Japan, National Institute for Materials Science.
 40. Faulkner R. G.: 'Microstructural examination of Ex-Heysham header creep specimens', Report MP/BEG/257, Loughborough University Enterprises Ltd. Loughborough, 2002.
 41. Gasca-Neri R., Ahlquist C. N. and Nix W. D.: 'A phenomenological theory of transient creep', *Acta Metall.*, 1970, 18, 655–661.
 42. Biberger M. and Gibeling J. C.: 'Analysis of creep transients in pure metals following stress changes', *Acta Metall. Mater.*, 1995, 43, 3247–3260.
 43. Morris D. G.: 'Creep in Type 316 stainless steel', *Acta Metall.*, 1978, 26, 1143–1151.
 44. Kroner E.: 'On the plastic deformation of polycrystals', *Acta Metall.*, 1961, 9, 155–161.
 45. Endo T., Shimada T. and Langdon T. G.: 'The deviation from creep by viscous glide in solid solution alloys at high stresses-I. Characteristics of the dragging stress', *Acta Metall.*, 1984, 32, 1991–1999.
 46. Cottrell A. H. and Jaswon M. A.: 'Distribution of solute atoms around a slow dislocation', *Proc. R. Soc. Lond. A*, 1949, 199, 104–114.
 47. Kofstad P.: 'High temperature oxidation of metals', 1966, New York, John Wiley & Son.
 48. Chevalier M. J.: 'Carburisation of type 316 stainless steel in an AGR environment: Status of current understanding', Report E/REP/BBGB/0120/AGR/13, EDF Energy Nuclear Generation Ltd; 2013, Barnwood, UK.
 49. Biglari F. and Nikbin K. M.: 'Environmental creep intergranular damage and multiscale crack evolution model for engineering alloys', *Comp. Mat. Sci.*, 2014, 84, 267–277.
 50. Webster G. A. and Ainsworth R. A.: 'High temperature component life assessment', 1994, London, Chapman & Hall.